coatings

MDPI

Article

Thermal Characterization of Coolant Maxwell Type Nanofluid Flowing in Parabolic Trough Solar Collector (PTSC) Used Inside Solar Powered Ship Application

Wasim Jamshed [1,*], Ceylin Şirin [2], Fatih Selimefendigil [2], MD. Shamshuddin [3], Yasir Altowairqi [4] and Mohamed R. Eid [5,6,*]

1 Department of Mathematics, Capital University of Science and Technology (CUST), Islamabad 44000, Pakistan
2 Department of Mechanical Engineering, Manisa Celal Bayar University, Manisa 45140, Turkey; cceylinsirinn@gmail.com (C.Ş.); fatih.selimefendigil@cbu.edu.tr (F.S.)
3 Department of Mathematics, Vaagdevi College of Engineering (Autonomous), Bollikunta, Warangal 506005, Telangana, India; shammaths@gmail.com
4 Department of Physics, College of Science, Taif University, P.O. Pox 11099, Taif 21944, Saudi Arabia; y.altowairqi@tu.edu.sa
5 Department of Mathematics, Faculty of Science, New Valley University, Al-Kharga 72511, Al-Wadi Al-Gadid, Egypt
6 Department of Mathematics, Faculty of Science, Northern Border University, Arar 1321, Saudi Arabia
* Correspondence: wasiktk@hotmail.com (W.J.); m_r_eid@yahoo.com (M.R.E.)

Citation: Jamshed, W.; Şirin, C.; Selimefendigil, F.; Shamshuddin, M.; Altowairqi, Y.; Eid, M.R. Thermal Characterization of Coolant Maxwell Type Nanofluid Flowing in Parabolic Trough Solar Collector (PTSC) Used Inside Solar Powered Ship Application. *Coatings* **2021**, *11*, 1552. https://doi.org/10.3390/coatings11121552

Academic Editors: Mikhail Sheremet and Yujun Song

Received: 24 November 2021
Accepted: 13 December 2021
Published: 17 December 2021

Abstract: Parabolic trough solar collectors (PTSCs) are generally utilized to reach high temperatures in solar-thermal applications. The current work investigates entropy production analysis and the influence of nano solid particles on a parabolic trough surface collector (PTSC) installed within a solar powered ship (SPS). For the current investigation, the non-Newtonian Maxwell type, as well as a porous medium and Darcy–Forchheimer effects, were used. The flow in PTSC was produced by a nonlinear stretching surface, and the Cattaneo–Christov approach was used to assess the thermal boundary layer's heat flux. Similarity transformation approach has been employed to convert partial differential equations into solvable ordinary differential equations allied to boundary conditions. Partial differential and the boundary conditions have been reduced into a group of non-linear ordinary differential equations. A Keller-box scheme applied to solve approximate solutions of the ordinary differential equations. Single-walled carbon nanotubes -engine oil (SWCNT-EO) and Multiwalled carbon nanotubes/engine oil (MWCNT-EO) nanofluids have been utilized as working fluid. According to the findings, the magnetic parameter led to a reduction in the Nusselt number, as well as an increment in skin friction coefficient. Moreover, total entropy variance over the domain enhanced for flow rates through Reynolds number and viscosity fluctuations were monitored by using Brinkman number. Utilizing SWCNT-EO nanofluid increased the thermal efficiency between 1.6–14.9% in comparison to MWCNT-EO.

Keywords: parabolic trough solar collector; maxwell nanofluid; Cattaneo–Christov model; Keller-box method

1. Introduction

Rapid growth of population and industrialization are constantly increasing the demand for energy [1]. Therefore, it is of utmost necessity to utilize sustainable and cost-effective energy sources to fulfill the demands of energy. Solar energy is one of the clean and inexhaustible energy sources that can be utilized in both electrical and thermal energy generation [2]. Parabolic trough solar collectors (PTSCs) are one of the effective methods of thermal utilization from solar energy [3]. PTSC applications are generally preferred to reach higher temperatures in comparison to flat-plate solar collector systems [4]. The thermal efficacy of a PTSC is affected by the thermophysical characteristics of the absorbing fluid, fluid velocity, and length of the collector [5–7]. Thermophysical characteristics of the working fluid in thermal systems can be enhanced by adding nano-sized particles suspended homogeneously [8,9]. These nano-sized particles have much larger surface areas and thus have great potential for heat transfer improvement [10]. Nanoparticles contain almost 20% of their electrons at the surface which makes them ready to transfer heat. Another benefit of utilizing nanofluids is particle agitation which causes micro-eddies to expand the hydrodynamic boundary layer and decrease the thickness of the thermal boundary layer to increase micro-convection between layers of fluid and heat transfer [11].

Photovoltaic thermal collectors, or PV collectors, are power production technologies that convert solar radiation into useable thermal and electrical energy. They are also known as hybrid solar collectors, photovoltaic thermal solar collectors, PV collectors, or solar cogeneration systems. One of the kinds of concentrated solar power (CSP) is PTSC. PV collectors combine photovoltaic solar cells, which convert sunlight into electricity, with a solar thermal collector, which transports the PV module's otherwise wasted waste heat to a heat transfer fluid. These technologies can achieve better overall efficiency than solar PV or solar thermal alone because they combine electricity and heat generation inside the same component. PV systems have the advantage of being dependable. Although both PV and CSP require sunshine to operate, CSP requires direct sunlight. During cloud cover, PV solar panels will still work, although to a lower level. This makes them more appealing in locations where cloud cover is widespread, like Spain in the winter. Another benefit of PV over CSP is the ease with which individual power-producing sites may be set up. Solar panels, an open area, and a transfer connection to the grid network are all that is required for PV systems. The photovoltaic effect generates power without the need for any moving parts. Mirrors, steam tanks, a turbine generating system, steam condensers, and perhaps thermal storage tanks are required for CSP systems. This complicates the building and operation of CSP plants compared to PV plants. PV's ease of usage makes it ideal for use in households and small businesses to reduce power costs. Personal usage of CSP is impractical due to its complexity and necessary space. It has been discovered that the use of solar energy in the maritime power system is widely regarded as a highly promising option for many countries, as it provides the way for the development of green ships. The integration of photovoltaic (PV) energy into the ship's power system necessitates an understanding of the electrical power system as well as many other aspects of shipping. The solar-powered ship has been invented by Raphaël Domjan, who started and finished the first-round trip around the world by utilizing solar energy among September 2010 and May 2012 and aboard the MS catamaran Planet Solar. In 2015, the first polar solar navigation in the Arctic Ocean has been carried out. He is the founder as well as the pilot of the project named Solar Stratos, the first solar plane which flew in the stratosphere. In August 2020, he jumped off of an electric plane and it is considered to be the first solar free fall. Sun et al. [12] probed the designing as well as the implementation of PV systems on ships. The characteristics based on the transient have been elaborated under two operative constraints: at ocean and seaport. A massive number of harmonics are created as soon as PV is incorporated into the ship's grid. The economic viability of putting PV systems aboard commerce ships has been investigated [13]. Sulaiman [14] investigated the viability of utilizing PV as backup power for Auxiliary Engines (AEs). Lee et al. [15] assessed the calculation of stability and investigated a mixture PV (diesel) ship style. In their paper [16], Babu and Jain investigated the use of PV systems on tiny distant-aquatic fishing boats in India. Cristea [17] demonstrated the testing results of the ship's PV panel. Kirkpatrick [18] examined the efficacy of PV systems on ships widely utilized in the Navy. Kobougias et al. [19] studied the requirements of a PV-based ship system. Utama et al. [20] investigated the solar-powered catamaran fishing craft. Yufang et al. [21] investigated the design of a fuel-free spacecraft powered by solar and wind energy. Alfonsín et al. [22] offered a first model based on a theory on the scheme of hybrid hydrogen as well as renewable energy to an electrical propulsive in the case of sailboats. Cristea et al. [23] researched the corresponding among computed and actual PV systems on the practice ship. They found that the level nominated PV panels to happen to be more efficient as compared to the vertical type. It has been observed that the capacitance of utilizing PV scheme on the ship is as a supplementary power to cut out the use of fossil fuel and it has been studied in [24]. Peng et al. [25] established a simulation model for a standard ship power-system and a computation scheme for PV model in PSCAD program. Lan et al. [26] proposed a procedure to decide the optimal volume of the PV-diesel-battery mixture scheme for the ship power processes for reducing the cost of capital, cost of fuel, and discharges from the exhaust. The author also studied the optimizing of slope-angle found in the PV-panels on a large oil hauler-ship. As the slope-angle increases, the production of the power of PV-panel decreases under the outcome of the investigation [27]. Tang et al. [28] have announced a system of power-management of the "CoscoTengfei" ship, it is united into PV system. The significance of low incidence quivering of a ship in the productivity appearances of PV-cells underneath varying solar-radiative is deliberated in [29]. Wen et al. [30] studied the PV-ESS-Diesel mixture-ship power-system when the ship is in motion. A charging station of an electrical ship along with a grid connection of natural resource energy is analyzed in [31]. The use of LabVIEW, as well as MATLAB for simulating ship power systems, has been shown in [32]. Tang et al. [33] performed PV matrix design with sophisticated MPPT control. Yuan et al. [34] showed a large-measurement PV system developed for "COSCO Tengfei" with a peak power of 143 kW. Figure 1 represents a solar-powered ship. Figure 1 represents a solar-powered ship [35].

Figure 1. Solar powered ship.

Numerical solution techniques are commonly used to evaluate thermal systems. They allow simulation and determine the thermal and flow structure of the analyzed case without conducting any experiment. Numerical approaches are also widely utilized for analyzing solar-thermal systems [36–38]. There is some research about the employment of nanoliquids in solar-systems. Ghasemi and Ahangar performed a numerical investigation of a PTSC with Cu/water nanofluid. According to their results, outlet temperature has been increased approximately 28% by utilizing nanofluid [39]. Subramani et al. [40] investigated a PTSC working with Al_2O_3/water nanofluid. Moreover, the effect of CNT coating on the performance of PTSC has been examined. Hachicha et al. [41] simulated PTSC utilizing MWCNT/water nanofluid at different seasonal conditions. According to their simulation results, the Nusselt number was improved by a maximum of 21% with the use of nanofluid. Bellos et al. [42] analyzed nanofluid-based PTSCs with EES software to upgrade the thermal performance. The simulation findings indicated that the maximum thermal enhancement was obtained approximately 4%–17% with the use of nanofluids and different modifications. In an investigation done by Abed et al. [43], the thermal performance of PTSC with non-uniform heating was investigated. They used six different non-metallic nanoparticles and three different base fluids in the study. Results showed that using nanofluids significantly improved thermal efficiency. Subhedar et al. [44] integrated a PTSC using nanofluid with single slope solar still. According to the results, utilized modifications improved the thermal efficiency by 70%. Bezaatpour et al. [45] developed a PTSC with rotary absorber tested the system by using nanofluids. The exergy efficacy of the PTSC was improved by 24% with the use of the modifications. Rejeb et al. [46] investigated PTSC-driven absorption refrigerators using nanofluids. COP value was increased between 12.5–15.5% with nano-additives. Peng et al. [47] empirically analyzed metal-based nanofluids in PTSCs system. Adding nanofluid to the system increased heat transfer by almost 45%. Minea and El-Maghlany [48] analyzed the effects of utilization of hybrid-nanofluid on the yield of PTSCs. In another study, O'Keeffe et al. [49] performed a transient simulation PTSC using nanofluid. Literature in connection with new developments in fluid flow in the light of different fluid model is enumerated in Refs. [50–64].

Exergy destruction and entropy generation comparatively grow stronger because of fluid friction and vibration, electrical resistance, mixing, and reactions. Irreversibility's bring about decrement in useful work and consequently, the energy gain rate from solar systems is ideally low. Correspondingly, exergy investigation is a crucial method for investigating the energy harvesting behavior of solar systems [65–67]. Ebrahimi-Moghadam et al. [68] analyzed a PTSC using alumina/ethylene glycol nanofluid for minimizing entropy growth. They utilized machine learning approaches in the investigations. According to the results, utilizing nanofluids led to decrease thermal entropy generation. Mwesigye et al. [69] numerically analyzed PTSC using nanofluid. As a result, the entropy growth rate decreased at low flow rate values. There are also some recent advancements in the field of entropy analysis of solar collectors available in the literature [70–72].

This source of power is very important in developing countries as solar energy is plentiful compared to other sources of energy. Advantages of solar-powered ships/boats are that they are environmentally friendly, cost-effective, eliminate sound pollution, are capable of charging continuously, can restore a boat's dying battery, can charge our devices, have less environmental impacts, and above all, they are highly reliable. Studies in the literature show the importance of detailed entropy and thermal investigation on solar-thermal systems. Moreover, the utilization of nanofluids in PTSCs is important to upgrade the performance of the system. In this study, a viscous Maxwell nanofluid passed over an infinite heat flux induced horizontal surface has been analyzed with Cattaneo–Christov model. Two different Maxwell nanofluids (SWCNT-EO and MWCNT-EO) were employed to upgrade the thermal performance of PTSC. In addition, this study focuses on the influences of dimensionless numbers on entropy generation. The schematic view of the analyzed PTSC in this research is demonstrated in Figure 2.

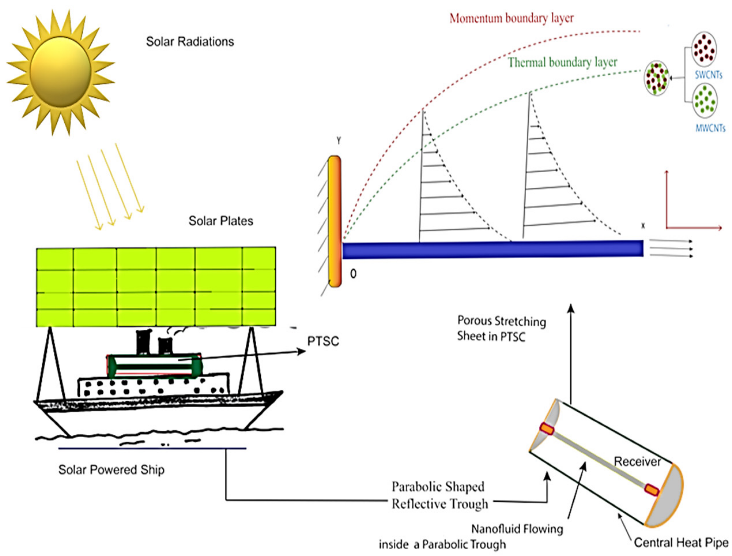

Figure 2. Schematic view of PTSC.

The major goal of constructing Figure 2 is to show the step-by-step approach for constructing the current theoretical model. Solar energy falls on the PTSC, passing through a fluid that is accompanied by thermal radiation and stores the maximum amount of energy on the PTSC through thermal conductivity. This energy is stored as heat energy, which is then turned into electrical energy with the use of photovoltaic cells in a batter. Inside the solar-powered spacecraft, this electrical energy is employed for a variety of reasons.

I. The sun's solar energy falls on the PTSC's cylindrical surface, and this energy is available in the form of heat energy. Because of the nanoparticles floating in the base fluid pass across PTSC, this energy has the greatest power. The incorporation of physical phenomena like thermal radiation and thermal conductivity increases the PTSC's heat storage capacity, which is the heart of the present theoretical experiment.

II. At the surface of PTSC, the greatest solar energy is stored in the form of thermal energy. The next step is to convert this energy into electrical energy, which will be utilized for navigation and electronic lighting. The solar cells battery, which is located within the fuel area box of the powered spacecraft, converts this heat energy into electrical energy. The battery stores energy throughout the day and uses it to power during the night.

III. The contribution of electrical energy to activities like as avionics, electric navigational lamps, and military communication is entirely reliant on the number of energies held or stored by the battery in terms of electrical energy.

2. Mathematical Formulation

The model with the non-uniform stretching velocity describes the moving flat solid surface:

$$U_w(x, 0) = bx \tag{1}$$

Here, b is the primary stretched ratio. The temperature of the insulated sheet is $¥_w(x, t) = ¥_\infty + b^* x$ and for ease of performance, it is measured to be firmed at $x = 0$, b^*, $¥_w$ and $¥_\infty$ stands for thermal difference rate, the wall temperature, and it's nearby. The surface is presumed to possess a slip effect and the surface is subjected to a temperature difference. The internal geometry of the PTSC is illustrated in Figure 3.

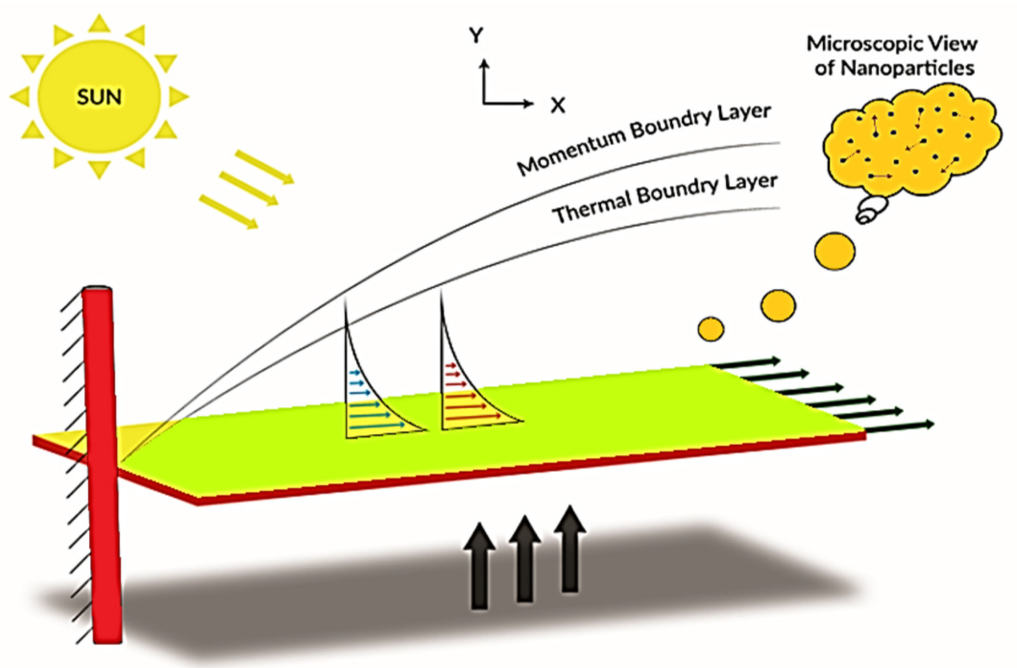

Figure 3. Schematic illustration of the flow model.

The modeling equations for conserved mass, flow, and thermal equations were considered as in Mukhtar et al. [73] modified with boundary layer claims adopted for 2D, steady flow conditions of Maxwell nanofluid along with porous medium, radiation heat flux, and Cattaneo–Christov heat flux are:

$$\frac{\partial v_1}{\partial x} + \frac{\partial v_2}{\partial y} = 0 \tag{2}$$

$$v_1 \frac{\partial v_1}{\partial x} + v_2 \frac{\partial v_1}{\partial y} = \frac{\mu_{nf}}{\rho_{nf}} \left[\frac{\partial^2 v_1}{\partial y^2} \right] - \lambda \left[{v_1}^2 \frac{\partial^2 v_1}{\partial x^2} + {v_2}^2 \frac{\partial^2 v_1}{\partial y^2} + 2 v_1 v_2 \frac{\partial^2 v_1}{\partial x \partial y} \right] - \frac{\mu_{nf}}{\rho_{nf} k} v_1 \tag{3}$$

$$\begin{aligned} v_1 \frac{\partial ¥}{\partial x} + v_2 \frac{\partial ¥}{\partial y} = & \frac{k_{nf}}{(\rho C_p)_{nf}} \left[\frac{\partial^2 ¥}{\partial y^2} \right] + \frac{1}{(\rho C_p)_{nf}} Q[¥ - ¥_\infty] + \frac{\mu_{nf}}{(\rho C_p)_{nf}} \left[\frac{\partial v_1}{\partial y} \right]^2 - \frac{1}{(\rho C_p)_{nf}} \left[\frac{\partial q_r}{\partial y} \right] \\ & -\Upsilon \left[v_1 \frac{\partial v_1}{\partial x} \frac{\partial ¥}{\partial x} + v_2 \frac{\partial v_2}{\partial y} \frac{\partial ¥}{\partial y} + v_1 \frac{\partial v_2}{\partial x} \frac{\partial ¥}{\partial y} + v_2 \frac{\partial v_1}{\partial y} \frac{\partial ¥}{\partial x} + {v_1}^2 \frac{\partial^2 ¥}{\partial x^2} \right. \\ & \left. + {v_2}^2 \frac{\partial^2 ¥}{\partial y^2} + 2 v_1 v_2 \frac{\partial^2 ¥}{\partial x \partial y} \right] \end{aligned} \tag{4}$$

The relevant boundary conditions are:

$$v_1(x,0) = U_w + N_w \left(\frac{\partial v_1}{\partial y} \right), v_2(x,0) = V_w, -k_0 \left(\frac{\partial ¥}{\partial y} \right) = h_f(¥_w - ¥) \tag{5}$$

$$v_1 \to 0,\ ¥ \to ¥_\infty \ as \ y \to \infty \tag{6}$$

Flow velocity holds in the form as $\overleftarrow{v} = [v_1(x,y), v_2(x,y), 0]$. ¥ is fluid temperature. The fluid relaxation and thermal relaxation factors are expressed as λ and Υ, respectively. Other potential parameters are, slip length (N_w), sheet penetrability (V_w), heat source (Q), heat transport factor (h_f), penetrability (k), and thermal conductance (k_0). Table 1 summarizes the material specifications for the Maxwell nanofluid [74–79].

Table 1. Thermo-physical attributes for Maxwell nanofluid [74–79].

Properties	Expression
Density	$\rho_{nf} = (1-\phi)\rho_{nf} + \phi\rho_s$
Dynamic viscidness	$\mu_{nf} = \mu_f (1-\phi)^{-2.5}$
Heat capacity	$(\rho C_p)_{nf} = (1-\phi)(\rho C_p)_{nf} + \phi(\rho C_p)_s$
Thermal conductivity	$\frac{k_{nf}}{k_f} = \left[\frac{[(k_f + (m-1)k_f) - \phi(m-1)(k_f - k_s)]}{[k_s + (m-1)k_f] + \phi(k_f - k_s)} \right]$

In Table 1, (ϕ) is nanoparticle fractional volume, ρ_f and ρ_s are fluid and particle density values, μ_f is dynamic viscosity, $(C_p)_f$ and $(C_p)_s$ are heat capacitance values of fluid and particle, κ_f and κ_s are thermal conductivities of fluid and particles. As the thickness of the non-Newtonian Maxwell nanofluid restrict the radiation to pass through after some extend, the Rosseland approximation [80] is adopted to model the radiation correctly as given below:

$$q_r = -\frac{4\sigma^*}{3k^*} \frac{\partial ¥^4}{\partial y} \tag{7}$$

In Equation (7), k^* stands for the absorption coefficient, σ^* describes Stefan Boltzmann number. The engine oil characteristics, SWCNT, and MWCNT nanoparticles are shown in Table 2 [81,82].

Table 2. Material specifications at 20 °C [81,82].

Material	ρ (kg/m^3)	C_p (J/kgK)	k (W/mK)
Engine oil (EO)	884	1910	0.14
SWCNT	2600	425	6000
MWCNT	1600	796	3000

3. The Solution for the Problem

The crucial step of solving this BVP (Equations (2)–(4)) is that to handle the PDEs. By engaging the similarity variables, it has been done smoothly and converted to simplified ODEs. Stream functions can be given as [83,84]

$$v_1 = \frac{\partial \psi}{\partial y},\ v_2 = -\frac{\partial \psi}{\partial x} \tag{8}$$

and similarity variables as:

$$\gamma(x,y) = \sqrt{\frac{b}{\nu_f}}y,\ \psi(x,y) = \sqrt{\nu_f b}xf(\gamma),\ \theta(\gamma) = \frac{¥ - ¥_\infty}{¥_w - ¥_\infty} \tag{9}$$

into Equations (2)–(4) we get

$$f'^2 - ff'' - \frac{f'''}{\phi_1\phi_2} + \xi_M\left(f^2 f''' - 2ff'f''\right) + \frac{1}{\phi_1\phi_2}K_M f' = 0 \tag{10}$$

$$\theta''\left(1 + \frac{1}{\phi_4}P_r N_M\right) + P_r\frac{\phi_3}{\phi_4}\left[f\theta' - f'\theta + \theta\frac{Q_M}{\phi_3} + \frac{E_M}{\phi_1\phi_3}f''^2 - \vartheta_M\left(f'^2\theta - f''\theta - f^2\theta^2 - ff'\theta''\right)\right] = 0 \tag{11}$$

with

$$\left.\begin{array}{c} f(0) = S,\ f'(0) = 1 + \Lambda_M f''(0),\ \theta'(0) = -B_\varepsilon(1 - \theta(0)) \\ f'(\xi) \to 0,\ \theta(\xi) \to 0,\ as\ \xi \to \infty \end{array}\right\} \tag{12}$$

ϕ'_i expression is $1 \leq i \leq 4$ in Equations (10) and (11) constitute the thermophysical aspects of the Maxwell nanofluid.

$$\left.\begin{array}{c} \phi_1 = (1-\phi)^{5/2},\ \phi_2 = \left(1 - \phi + \phi\frac{\rho_s}{\rho_f}\right),\ \phi_3 = \left(1 - \phi + \phi\frac{(\rho C_p)_s}{(\rho C_p)_f}\right) \\ \phi_4 = \left(\frac{(k_s+2k_f)-2\phi(k_f-k_s)}{(k_s+2k_f)+\phi(k_f-k_s)}\right) \end{array}\right\} \tag{13}$$

As the Equation (2) satisfied identical, the notation ($'$) used for representing the derivatives concerning γ. Here, $\xi_M = b\lambda$ (Non-Newtonian Maxwell), $\vartheta_M = b\vartheta_0$ (relaxation time parameter) and $K_M = \frac{\nu_f}{bk}$ (porous medium) parameters defined along with $\vartheta_M = b\lambda_0$ (relaxation time), $Pr = \frac{\nu_f}{\alpha_f}$ (Prandtl number), $\alpha_f = \frac{\kappa_f}{(\rho C_p)_f}$ (thermal diffusivity), $S = -V_w\sqrt{\frac{1}{\nu_f\,b}}$ (mass transfer), $Q_M = \frac{Q_0}{(\rho C_p)_f b}$ (heat source), $N_M = \frac{16}{3}\frac{\sigma^* ¥_\infty^3}{\kappa^*\nu_f(\rho C_p)_f}$ (thermal radiation), $\Lambda_M = \sqrt{\frac{b}{\nu_f}}N_w$(velocity slip), $E_M = \frac{U_w^2}{(C_p)_f(T_w - T_\infty)}$ (Eckert number) and $B_\varepsilon = \frac{h_f}{k_0}\sqrt{\frac{\nu_f}{b}}$ (Biot number) parameters, respectively.

Other two physically vital parameters like skin level friction $\left(C_f\right)$ and the reduced Nusselt number (Nu_x) can be stated as [73]:

$$C_f Re_x^{\frac{1}{2}} = \frac{f''(0)}{(1-\phi)^{2.5}},\ Nu_x Re_x^{-\frac{1}{2}} = -\frac{k_{nf}}{k_f}(1 + N_M)\theta'(0) \tag{14}$$

where $Re_x = \frac{U_w x}{\nu_f}$ is the local Reynolds number.

The non-dimensional entropy formation in nanofluids is expressed as [85]:

$$N_G = Re\left[\phi_5(1 + N_M)\theta'^2 + \frac{1}{\phi_1}\frac{B_M}{\Omega}\left(f''^2 + K_M f'^2\right)\right] \tag{15}$$

Here, Re is the Reynolds number, Ω is the thermal gradient and B_M is the Brinkman number.

4. Numerical Technique

This chapter is intended to the numerical solution of the law of momentum and heat Equations (10) and (11), subject to Equation (12), utilizing the Keller-box technique [85]. The authors chose this technique due to the scheme is second-order convergent and unconditionally stable.

The Keller-box technique is made up of the following stages:

- The controlling equations must first be formulated as a set of first-order equations.
- The domain is discretized once the order of equations is reduced, allowing us to calculate the estimated solution across each subdomain rather than the full domain. This produces more accurate findings.
- Central difference derivatives and the average of function mid-points are utilized to create finite-difference equations.
- The outcoming formulas are then linearized utilizing Newton's technique and written in tridiagonal matrix form, as Keller explained.
- Finally, the outcome is obtained by LU analysis.

The flow chart of KBM is shown in Figure 4.

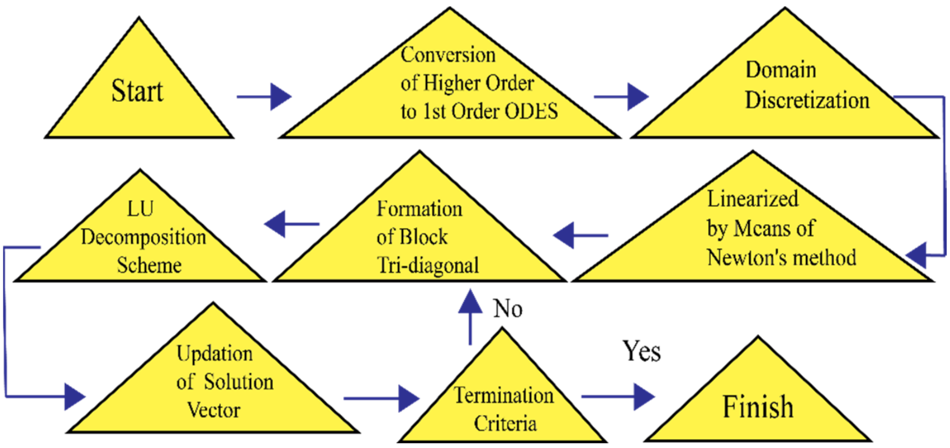

Figure 4. Flow chart of Keller-box method.

5. Code Validation

The validity of the computational technique was determined by comparing the heat transmission rate from the current approach to the verified results of earlier studies [86,87]. A comparison of the results of the current study with the results of the previous study is shown in Table 3. The current study is comparable and presented highly accurate results.

Table 3. Comparing $-\theta'(0)$ with alteration in Prandtl number, and taking $\phi = 0$, $\vartheta_M = 0$, $\Lambda_M = 0$, $N_M = 0$, $B_\varepsilon \to \infty$, $Q_M = 0$, $E_M = 0$ and $S = 0$.

Pr	**Wang [86]**	**Gorla & Sidawi [87]**	**This Study**
0.20	0.1691	0.1691	0.1691
0.70	0.4539	0.4539	0.4537
2.00	0.9114	0.9114	0.9114
7.00	1.8954	1.8954	1.8958

6. Results and Discussion

Set of differential Equations (9) and (10) with connected boundary conditions is solved numerically via Keller-box technique. Since the problem under investigation depends on dimensionless key parameters, their physical significance on flow characteristics, entropy generation, and substantial quantities are illustrated via plots and deliberated in detail with physical significance.

6.1. Effect of Maxwell Parameter (ξ_M)

The complete significance of the Deborah number (ξ_M) against the flow, thermal and entropy distributions of Maxwell nanofluid are portrayed in Figure 5a–c. Initially, Figure 5a is portrayed to see the impact of the Deborah number (ξ_M) for flow distribution, which manifests the descending (downward) behavior for flow curves of viscoelastic liquid. Mathematically, Deborah number (ξ_M) depends on elasticity and viscosity. Physically, the elastic property boosts up with an escalation in (ξ_M) and as a result, more resistance produces in a fluid motion and therefore velocity profile of fluid deteriorates. Additionally, an intensification in the magnitude of ξ_M corresponds to increases more kinetic energy because of this friction between nanoparticles increases and hence, thermal profile rate of Maxwell fluid boosts up as shown in Figure 5b, i.e., diminution inflow profiles of Maxwell fluid is detected with intensification in whereas opposite behavior is being noticed for temperature profiles. The physical behavior of entropy generation number for dimensionless Deborah number (ξ_M) is seen graphically in Figure 5c. It indicates a decrement in N_G close to the surface while a small increment is noticed at a distance from its as values of ξ_M elevates, later curves behave differently. The reason is the occurrence of a large temperature gradient at the surface which results in more entropy generation causes fluctuations in the motion of the particles.

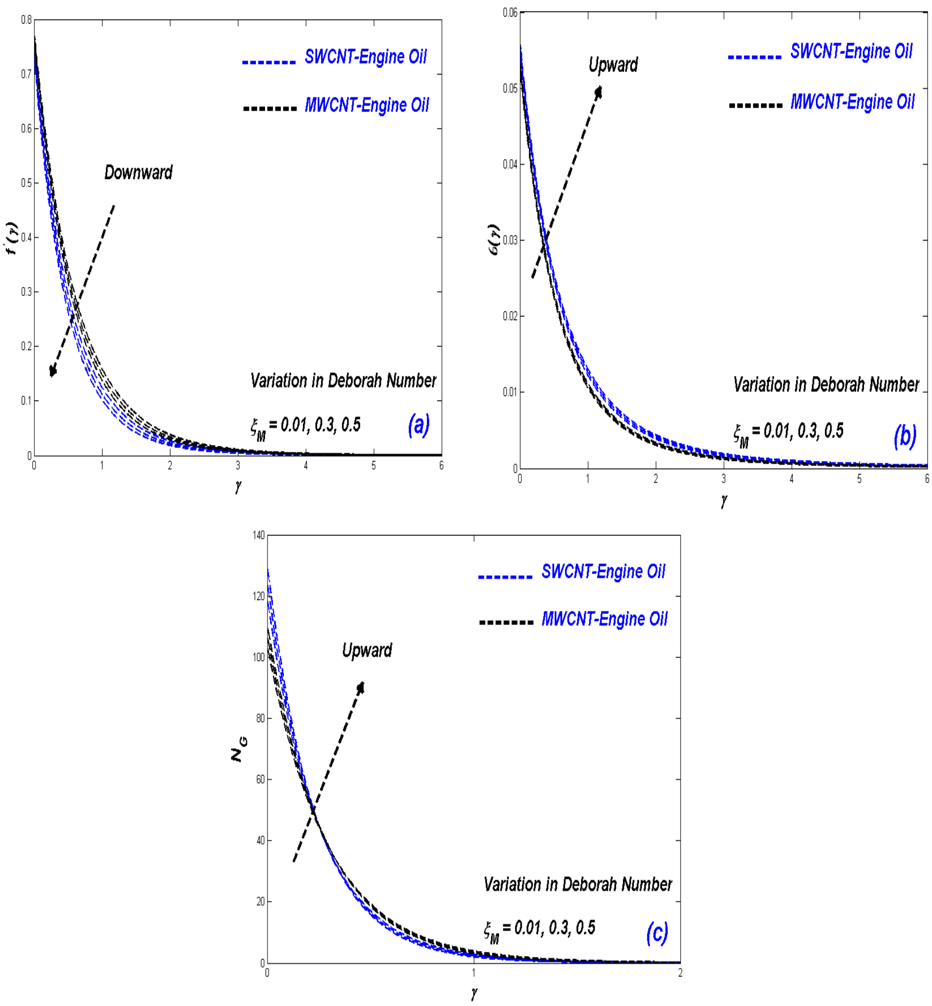

Figure 5. (**a**) Velocity change with ξ_M; (**b**) Temperature change with ξ_M; (**c**) Entropy change with ξ_M.

6.2. Impact of Porous Media Parameter (K_M)

Figure 6a–c shows the effects of inverse permeability parameter (K_M) on Maxwell nanofluid suspended in SWCNT and MWCNT with Engine oil s base fluid boundary layer regime on the stretching sheet. The flow velocity reduces as the modified permeability parameter is enhanced. According to this Figure 6a, it is understood that proliferation in permeability of porous medium reduces the flow rate through the porous medium and it consequently drags the velocity while providing resistance near the wall surface. It is because of reality that a rise in the porous term decreases nanoparticle collision due to a significant boost in the flow pore that in turn discourages heat generation. The viscous force controls the buoyancy force, thereby damping the flow magnitude. An opposite response is observed in Figure 6b, a rise in porosity term enhances the flow temperature. The viscosity of the carbon nanofluids is repressed as a free flow of the conducting nanoliquid is assisted, as SWCNT/Engine oil dominates the flow temperature when compared to MWCNT/Engine oil, but the opposite trend is observed for the velocity distribution. This is probably associated with both the density and viscosity of the respective carbon tube nanofluids and the re-distribution in the momentum component. The variation in entropy generation number N_G aginst K_M is depicted in Figure 6c, which indicates an increment in N_G close to the surface while a small decrease is noticed at a distance from its as values of K_M elevates. The reason is the occurrence of a large temperature gradient at the surface which results in more entropy generation. Judicious selection of the porous medium permeability may therefore provide an excellent mechanism for regulating the coating flow characteristics in industrial applications. It is also likely that greater permeability associated with larger pore spaces, permits better percolation of the suspended carbon nanoparticles and this enhanced mobility contributes to a reduction in friction at the stretching surface. We observe smooth and asymptotically smooth profiles with the free stream, validating the Keller-box numerical solution's prescription of a large infinity boundary condition.

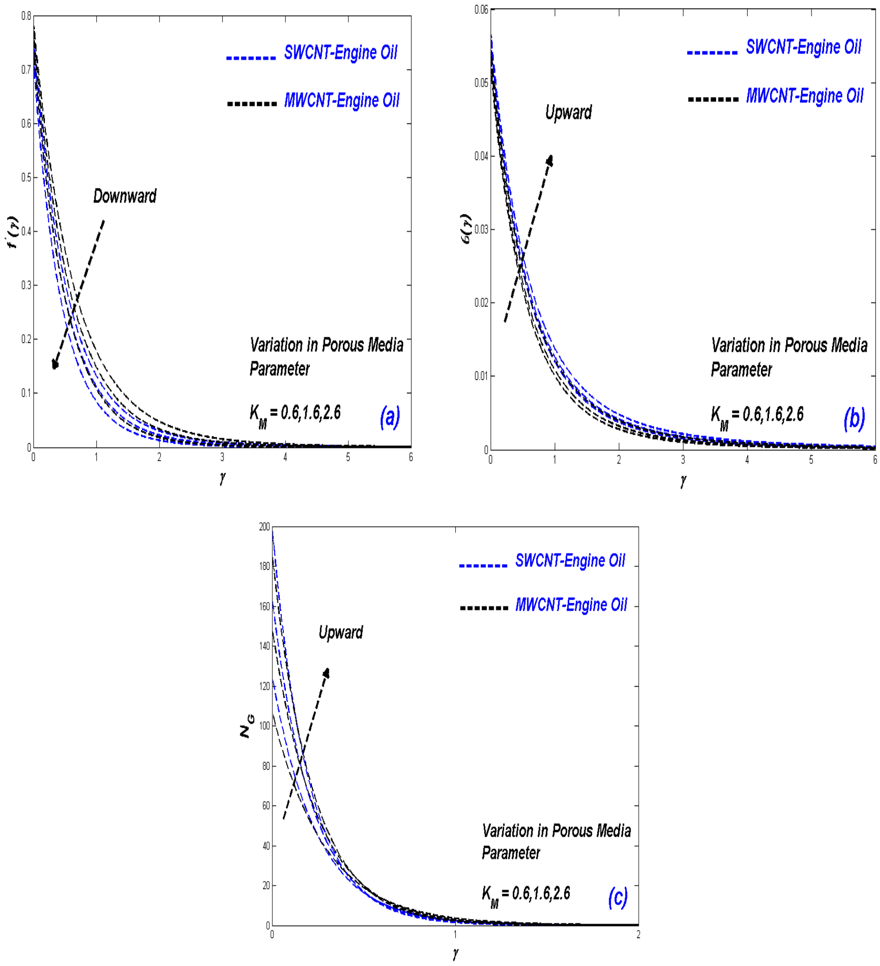

Figure 6. (**a**) Velocity change with k_M; (**b**) Temperature change with k_M; (**c**) Entropy change with k_M.

6.3. *Effect of Velocity Slip Parameter* (Λ_M)

Sensitivity of the stretching velocity slip parameter Λ_M obtained from boundary conditions is investigated and established on the flow fluid momentum and temperature distributions as revealed in Figure 7a–c. The progressive values of the velocity slip parameter Λ_M increased fluid viscosity and hence the velocity of fluid gets declined (Figure 7a). The results aligned well with the existing literature, as seen, the moving boundary sheet stimulates the single and multi walls of considered base fluids' thermal conductivity (Engine oil). The CNTs nanoliquid heat conduction strength is boosted by the stretching velocity term that enhances the fluid particle heat transfer. In the consideration of Maxwell nanofluid, heat transfer in the system increases as the stretching velocity parameter rises due to the high propagation of heat by the carbon nanofluid inspire temperature field. SWCNT/Engine oil dominates the flow temperature when compared to MWCNT/Engine oil as observed in (Figure 7b). The variation in entropy generation number N_G against velocity slip parameter Λ_M is depicted in Figure 7c. The graphical behavior of N_G aginst progressive values of velocity slip parameter Λ_M explores that it is insensitive (effective decrease) to vary at the surface as compared to away from it. Generally, no-slip conditions produce large velocity and temperature gradients due to which entropy generation shows high values close to the sheet. In our current study, slip condition at velocity implemented due to which entropy generation shows a gradual reduction close to the stretching walls (see Figure 7c).

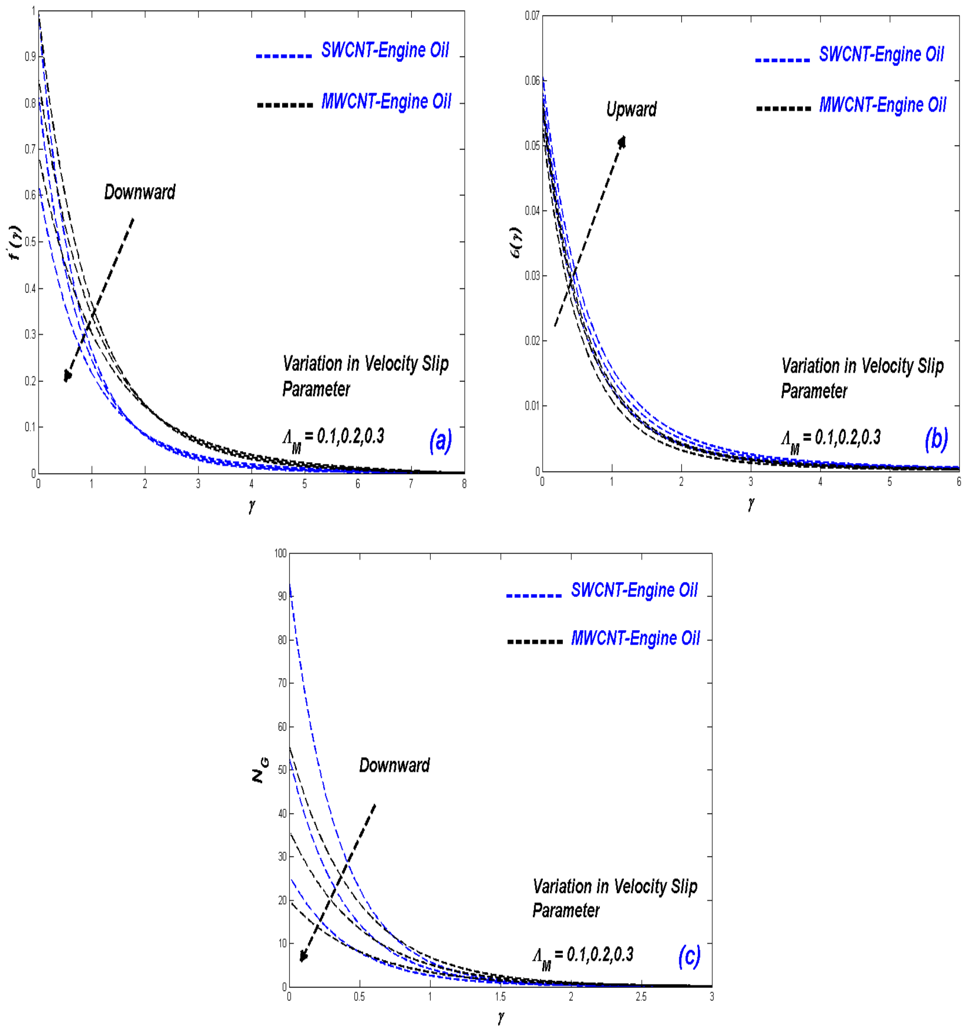

Figure 7. (**a**) Velocity change with Λ_M; (**b**) Temperature change with Λ_M; (**c**) Entropy change with Λ_M.

6.4. Impact of Nanoparticle Fractional Volume Parameter (ϕ)

In the occurrence of carbon suspended nanofluid, the impact of nanomaterial term (ϕ) on the flow characteristics (velocity, temperature, and entropy) is established in Figure 8a–c. As observed, rising volume fraction discourages the flow velocity profile and encourages the temperature field. The dimensional features of velocity magnitudes decrease all over the region due to low thermal boundary viscosity film that allows quick dissipation of heat out of the system to diminish the heat within the flow structure as observed from Figure 8a. The heat transfer of solid suspension nanoparticles of the working fluid is enhanced in the system, as such, the liquid bonding force is dampened. The flow distributions indeed present nanofluid material as a strong heat transfer convection and conduction coefficient. Hence, nanofluids are heat transfer forces in propelling the main industrial and technological advancement in this period. Therefore, as reported for Figure 8b nanomaterial term increases the energy distribution. Physically, in an ideal solution, volume concentration coincides with the volume fraction of the nanoliquid, hence the solution volume is equal to total carbon nanotube constituent volume. In the considered base fluid, the multiple and single carbon nanotube walls velocity is damped the molecular diffusion and less collision of nanoparticles in the moving boundless medium. The respective influence of variation in the nanomaterial term on the entropy generation is described in Figure 8c. In a process where irreversibility is in existence, entropy generation is defined. This measures the amount of energy loss that causes degradation of technology system performance. As seen, the parameters encourage system irreversibility due to high energy dissipation near the stretching plate as the values of the parameters are raised. However, the irreversibility due to chemical diffusivity, friction, and conducting heat regularly decrease a few distances from the moving surface because the fluid thermodynamic equilibrium is rising gradually and continuously toward the free field. The decrease in the entropy generation continues until a balance thermodynamic equilibrium is attained and energy dissipation tends to zero. This parameter enables the doping of the nanoparticle to be simulated in the circulating fluid in the enclosure. With increasing volume fraction, the entropy generation is intensified at the stretching walls. Conforming that increasing nanoparticle presence in the nanofluid achieves the desired thermal enhancement.

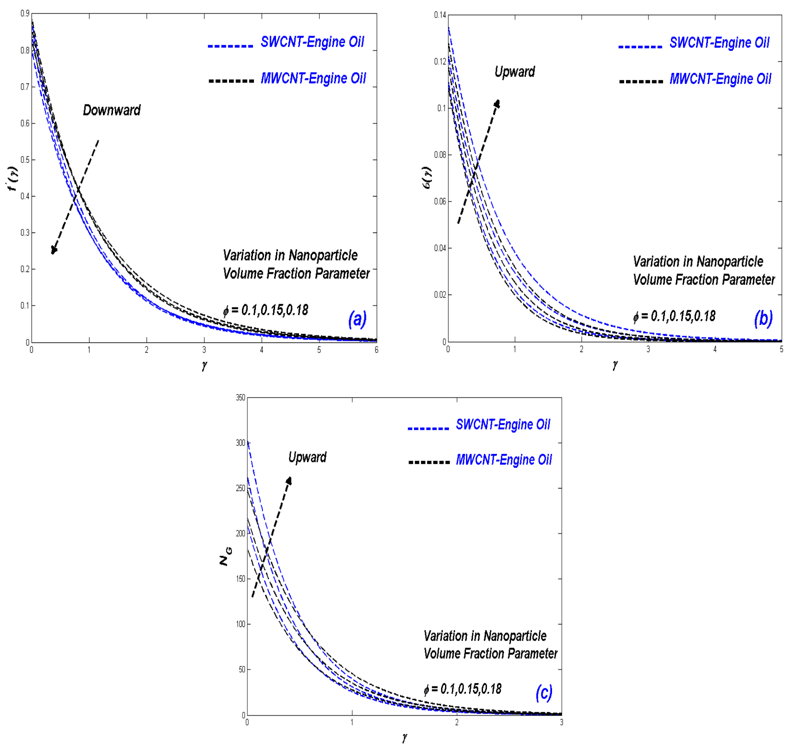

Figure 8. (**a**) Velocity change with ϕ; (**b**) Temperature change with ϕ; (**c**) Entropy change with ϕ.

6.5. Impact of Radiative Heat Flux Parameter, Relaxation Time Parameter, Eckert Number, and Heat Source Parameter

Figure 9a shows the results of changes in temperature distributions under different values of heat flux parameter (N_M). It was remarked that the mean flow temperature outline upsurges for an increment in N_M increases. Physically, although the thermal radiation parameter is increased, the radiative flux stimulates the nano-polymeric wave, which adds thermal energy to the process. In addition, when compared to the heat transmission of conductivity, the heat transmission of radiation declines less the buoyancy force and thermal boundary-layer thickener. As a result of this temperature, the boundary layer strengthens. Entropy generation impact on the nanofluid motion of radiation parameter N_M pictured in Figure 9b for both types of SWCNT/Engine oil and SWCNT-MWCNT/Engine oil nanoparticles. It is examined that increasing values of radiation parameter (N_M) gradual increase in entropy distribution. At different significance, the radiation parameter vigorously influenced the entropy rate in the stretching porous device as observed in Figure 9b. The results presented in Figure 10a demonstrated the strength of the rising relaxation parameter (ϑ_M) on the flow of temperature to a monotonically increased stream term γ. It displays that the intensified thermal relaxation parameter declines the thermal distribution and the temperature boundary layer of Maxwell nanofluid. It happens because more time is needed to transfer heat waves in nanoliquid for a higher extent of thermal relaxation time scale and therefore, the heat in a material transforms sluggishly. Hence the thermal distribution of the Maxwell nanoliquid lessens. Figure 10b show the variation in Entropy with relaxation parameter (ϑ_M). Intensified relaxation parameter significantly accelerates the entropy distribution, at different significance, the relaxation parameter vigorously influenced the entropy rate in the stretching porous device, overall rising in the magnitude of the thermal relaxation parameter is because of the increasing rate in the heat transfer in the non-Newtonian viscoelastic fluid regime. Physical behavior of heat distribution and entropy generation number for dimensionless parameter Eckert number (E_M) is seen graphically in Figure 11a, b. The variation in temperature distribution against E_M is depicted in Figure 11a. When the kinetic energy of the nanofluid is greater than its internal energy, the convective motion becomes more important, consequently, we w an increase in the nanofluid temperature. This is well presented in Figure 11a, where the growth in the Eckert number leads to strong growth in temperature. Even small values of the Eckert number exert a significant influence on the thermal field. Dissipation effects correspond to substantial heat generation in the regime and this manifests in temperature elevations to a monotonically increased stream term. Furthermore, Figure 11b depict the variation in N_G against values of Eckert number (E_M). This indicates an increase in N_G by enhancing Eckert number (E_M) initially. Physically, the increment in the molecular motion and kinetic energy is due to the increment has been the crucial factor in the ascent in the profile of entropy generation. In addition, it is worth mentioning that the amount of entropy in the SWCNT/EO phase has been more than that of the MWCNT/EO. At different significance far from the stream, the Eckert number vigorously behaves in opposite behavior and influenced the entropy rate in the stretching porous device as observed in Figure 11b. This is appropriate for a screw extruder, where the energy provided to the polymer melt originates from the viscous heat created by shear forces between components of the liquid moving at various velocities. The response of heat distribution and entropy generation to heat generation is established in Figure 12a,b. An increase in heat generation enhances the temperature field in a stretchable boundless device. The observation reveals that the heat generation term stimulates the energy equation terms of the Maxwell nanofluid. It is because little-or-no heat diffused out of the non-Newtonian viscoelastic system to the surrounding. This is because the temperature boundary layer is stimulated that in turn discourages the diffusion in the stretching device. In the energy equation, the heat production parameters are propelled to inspire heat generation within the Maxwell nanofluid which leads to a general rise in the heat profiles. Therefore, the heat generation parameters omit radiations and create more quantity of heat in the fluid, and finally, the temperature curves of the nanoliquid escalate. Figure 12b represents the effect of heat generation effects far from the stretching sheet which escalates the amount of entropy which is due to a rise in temperature.

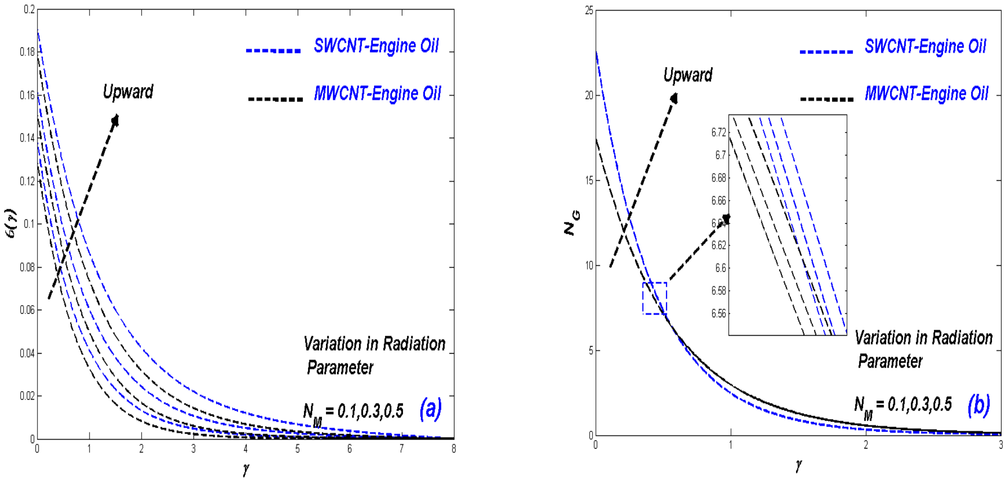

Figure 9. (**a**) Temperature change with N_M; (**b**) Entropy change with N_M.

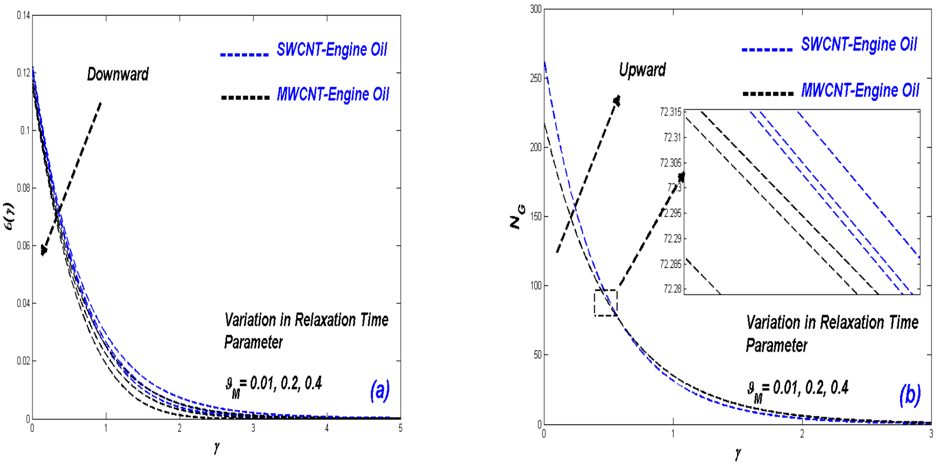

Figure 10. (**a**) Temperature change with ϑ_M; (**b**) Entropy change with ϑ_M.

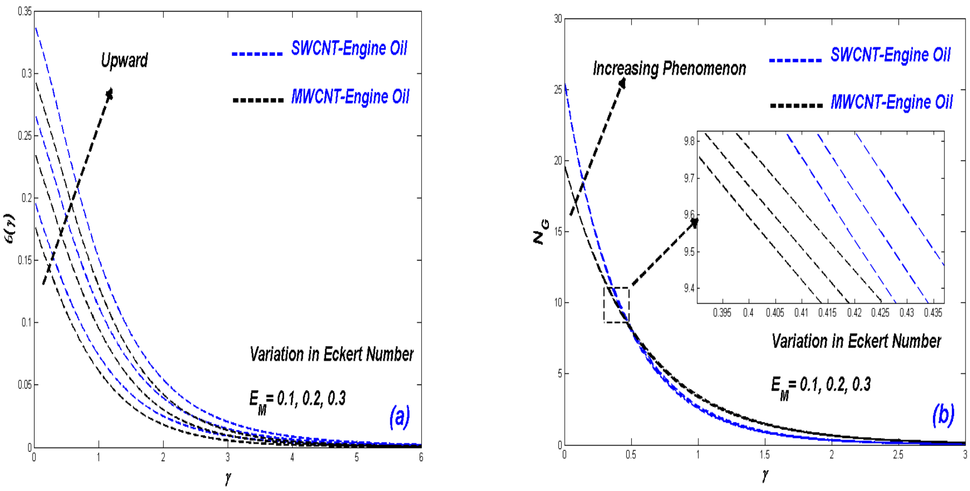

Figure 11. (**a**) Temperature change with E_M; (**b**) Entropy change with E_M.

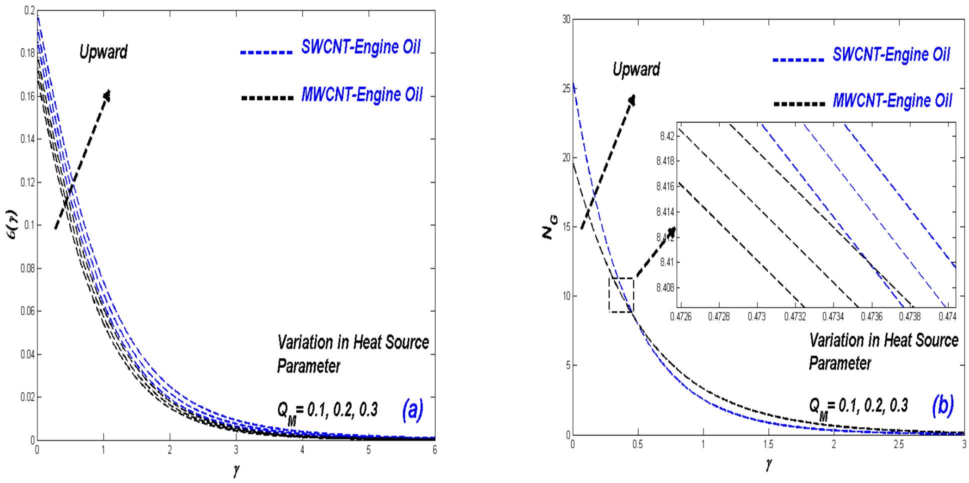

Figure 12. (**a**) Temperature change with Q_M; (**b**) Entropy change with Q_M.

6.6. Influence of Reynolds and Brinkman Numbers on Entropy Generation

Figure 13a, b are plotted to enlighten the influence of Reynolds and Brinkman numbers (R_e and B_M). Towards entropy generation distribution in the stretching boundary layer regime. It is seen that the greater the values of Reynolds Number (R_e) boosts the entropy effect. The retrogression of frictional forces tends to gasify the entropy profiles due to greater values of Reynolds Number (R_e). Figure 13b depicts the variation in entropy generation number N_G against the values of Brinkman Number (B_M) which indicates an increase in entropy generation by enhancing Brinkman Number (B_M). Such behavior, Brinkman Number (B_M) explores the viscous effect of the fluid. Hence, high values of Brinkman Number (B_M) show a dominant effects of fluid friction which is a strong source of entropy generation. The graphical behavior of N_G against pertinent parameters (Figure 13a,b) shows that the variation sensitivity at the surface as compared to away from it.

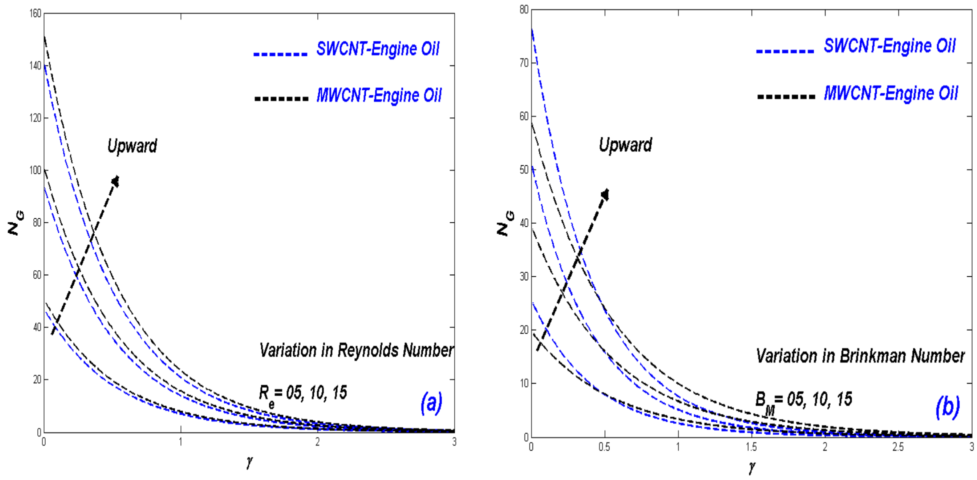

Figure 13. (**a**) Entropy changes with R_e; (**b**) Entropy change with B_M.

6.7. Relative Heat Transfer Rate in SWCNT-EO and MWCNT-EO Nanofluids

For stable values of nanoparticle concentration of SWCNT and MWCNT, it is observed that the SWCNT-EO nanofluid is a more effective transfer source in comparison to the MWCNT-EO nanofluid. SWCNT possessed an upper hand in thermal conductivity over that of MWCNT. This also reflects in the heat transfer rates in Table 4, that SWCNT-EO nanofluid has a better heat transmission rate in a comparing to MWCNT-EO nanofluid through the Nusselt number variations for physical parameters of this work.

Table 4. Skin friction ($C_f Re_x^{1/2}$) and Nusselt Number ($N_u Re_x^{-1/2}$) values for $Pr = 6450$.

ξ_M	K_M	Q_M	ϑ_M	ϕ	Λ_M	B_ε	N_M	E_M	$C_f Re_x^{1/2}$ SWCNT-EO	$C_f Re_x^{1/2}$ MWCNT-EO	$N_u Re_x^{-1/2}$ SWCNT-EO	$N_u Re_x^{-1/2}$ MWCNT-EO	Relative $\frac{Nu_{(SWCNT)}-Nu_{(MWCNT)}}{Nu_{(SWCNT)}}\times 100\%$
0.01	0.6	0.3	0.2	0.18	0.1	0.1	0.3	0.1	2.5826	2.3208	0.1726	0.1638	5.0%
0.3									2.6762	2.4239	0.1569	0.1409	10.1%
0.5									2.7442	2.4631	0.1488	0.1279	14.0%
	0.6								2.5826	2.3208	0.1726	0.1638	5.0%
	1.6								2.7734	2.5285	0.1623	0.1401	13.6%
	2.6								2.9345	2.7110	0.1484	0.1262	14.9%
		0.1							2.5826	2.3208	0.1935	0.1899	1.8%
		0.2							2.5826	2.3208	0.1851	0.1788	3.4%
		0.3							2.5826	2.3208	0.1726	0.1638	5.0%
			0.01						2.5826	2.3208	0.1632	0.1563	4.2%
			0.2						2.5826	2.3208	0.1726	0.1638	5.0%
			0.4						2.5826	2.3208	0.1843	0.1739	5.6%
				0.1					2.1446	1.9783	0.1927	0.1895	1.6%
				0.15					2.2437	2.2127	0.1896	0.1806	4.7%
				0.18					2.5826	2.3208	0.1726	0.1638	5.0%
					0.1				2.5826	2.3208	0.1726	0.1638	5.0%
					0.2				2.3663	2.2235	0.1510	0.1409	6.6%
					0.3				1.9829	1.8412	0.1382	0.1223	11.5%
						0.1			2.5826	2.3208	0.1726	0.1638	5.0%
						0.2			2.5826	2.3208	0.1623	0.1522	6.2%
						0.3			2.5826	2.3208	0.1491	0.1331	10.7%
							0.1		2.5859	2.3025	0.1923	0.1830	4.8%
							0.3		2.5859	2.3025	0.1726	0.1638	5.0%
							0.5		2.5859	2.3025	0.1652	0.1511	8.5%
								0.1	2.5859	2.3025	0.1726	0.1638	5.0%
								0.2	2.5859	2.3025	0.1581	0.1439	8.9%
								0.3	2.5859	2.3025	0.1343	0.1208	10.0%

7. Conclusions

The resented work aims to observe entropy production outline and Maxwell nanomoleculars' influence on thermal distribution in parabolic trough solar collector placed into a solar-powered ship by a stretched sheet. Catteneo–Chirstov effects have been utilized to investigate the mechanism of heat transfer and discussed on employing non-Newtonian Maxwell fluid model. In addition, our theoretical study depends on thermal physical properties, entropy, and solar radiation over a stretching surface. There are many applications for the structure, including photo-voltaic cells, solar-energy plates, solar streetlights, and solar-water pumps. The analysis begins with a mathematical formulation of the base flow from modified Navier–Stokes heat equations. The obtained ordinary differential equations are then solved by using a well-established Keller-box method in a computational tool MATLAB. The findings of this study quantitatively satisfied the existing ones in the literature, the summary of the novelty outcomes of this investigation is given as follows:

- SWCNT/EO nanofluid phase is observed to achieve superior thermal radiative enhancement relative to MWCNT/EO nanofluid phase.
- Increasing Deborah number (ξ_M), porous media parameter (K_M), velocity slip parameter Λ_M, nanomaterial term (ϕ), and relaxation time (ϑ_M) produces a significant diminution in the velocity field.
- Velocity slip parameter has a negative effect on velocity and entropy but opposite in temperature distribution.
- In the presence of nanomaterials, radiative, viscidness dissipative flow, and heat generation, the thickener of the thermal boundary-layer increases with time, which results in a diminished heat exchange rate.
- Plots for entropy generation number against radiative flux, relaxation time, Eckert number, and heat generation explore dual behavior.
- Porosity, heat generation, enthalpy, and solar radiation have an important role in the improvement of heat phenomena.
- Relative heat transfer rate is strongly elevated with greater porous medium permeability (1.6% to 14.9%).

Regardless of any physical parameters, SWCNT gives a preferable heat transfer compared to MWCNT. The current study has also demonstrated that Keller-box numerical method is a powerful computational approach for solving nonlinear rheological multi-physical nanofluid flow problems. The present simulations have been confined to steady-state conditions and carbon nanotubes. Future investigations will consider ferromagnetic nanoparticles and homogenous reaction effects and will be elaborated imminently.

Author Contributions: Conceptualization, W.J. and M.R.E.; methodology, W.J., C.Ş., F.S. and M.R.E.; software, W.J. and F.S.; validation, W.J. and M.R.E.; investigation, W.J., M.S. and M.R.E.; resources, Y.A. and M.R.E.; visualization, W.J. and M.R.E.; writing—original draft preparation, W.J.; writing—review and editing, C.Ş., F.S., M.S., Y.A. and M.R.E.; supervision, W.J.; project administration, M.R.E. and Y.A.; funding acquisition, Y.A. All authors have read and agreed to the published version of the manuscript.

Funding: This research received no external funding.

Institutional Review Board Statement: Not applicable.

Informed Consent Statement: Not applicable.

Data Availability Statement: The results of this study are available only within the paper to support the data.

Acknowledgments: Taif University Researchers Supporting Project number (TURSP-2020/249), Taif University, Taif, Saudi Arabia.

Conflicts of Interest: The authors declare no conflict of interest.

References

1. Tuncer, A.D.; Sözen, A.; Afshari, F.; Khanlari, A.; Şirin, C.; Gungor, A. Testing of a novel convex-type solar absorber drying chamber in dehumidification process of municipal sewage sludge. *J. Clean. Prod.* **2020**, *272*, 122862. [CrossRef]
2. Bayrak, F.; Oztop, H.F.; Selimefendigil, F. Experimental study for the application of different cooling techniques in photovoltaic (PV) panels. *Energy Conver. Manag.* **2020**, *212*, 112789. [CrossRef]
3. Ktistis, P.K.; Agathokleous, R.A.; Kalogirou, S.A. Experimental performance of a parabolic trough collector system for an industrial process heat application. *Energy* **2021**, *215*, 119288. [CrossRef]
4. Jaaz, A.H.; Hasan, H.A.; Sopian, K.; Ruslan, M.H.B.H.; Zaidi, S.H. Design and development of compound parabolic concentrating for photovoltaic solar collector: Review. *Renew. Sustain. Energy Rev.* **2017**, *76*, 1108–1121. [CrossRef]
5. Bellos, E.; Tzivanidis, C. Alternative designs of parabolic trough solar collectors. *Prog. Energy Combust. Sci.* **2018**, *71*, 81–117. [CrossRef]
6. Fredriksson, J.; Eickhoff, M.; Giese, L.; Herzog, M. A comparison and evaluation of innovative parabolic trough collector concepts for large-scale application. *Sol. Energy* **2021**, *215*, 266–310. [CrossRef]
7. Mahian, O.; Kianifar, A.; Kalogirou, S.A.; Pop, I.; Wongwises, S. A review of the applications of nanofluids in solar energy. *Int. J. Heat Mass Transf.* **2013**, *57*, 582–594. [CrossRef]
8. Khanlari, A.; Sözen, A.; Variyenli, H.İ.; Gürü, M. Comparison between heat transfer characteristics of TiO_2/deionized water and kaolin/deionized water nanofluids in the plate heat exchanger. *Heat Transf. Res.* **2019**, *50*, 435–450. [CrossRef]
9. Sözen, A.; Gürü, M.; Khanlari, A.; Çiftçi, E. Experimental and numerical study on enhancement of heat transfer characteristics of a heat pipe utilizing aqueous clinoptilolite nanofluid. *Appl. Therm. Eng.* **2019**, *160*, 114001. [CrossRef]
10. Badali, Y.; Koçyiğit, S.; Aytimur, A.; Altındal, Ş.; Uslu, I. Synthesis of boron and rare earth stabilized graphene doped polyvinylidene fluoride (PVDF) nanocomposite piezoelectric materials. *Polym. Compos.* **2019**, *40*, 3623–3633. [CrossRef]
11. Çiftçi, E. Simulation of nucleate pool boiling heat transfer characteristics of the aqueous kaolin and bauxite nanofluids. *Heat Transf. Res.* **2021**, *52*, 77–92. [CrossRef]
12. Sun, Y.W.; Yan, X.P.; Yuan, C.Q.; Lei, C.W. Research progress in marine grid-connected photovoltaic technology. In Proceedings of the 47th Annual Conference of the Australian and New Zealand Solar Energy Society (ANZSES), Townsville, Australia, 29 September–2 October 2009.
13. Glykas, A.; Papaioannou, G.; Perissakis, S. Application and cost–benefit analysis of solar hybrid power installation on merchant marine vessels. *Ocean Eng.* **2010**, *37*, 592–602. [CrossRef]
14. Sulaiman, O. Feasibility of using solar as a supporting hybrid power system for marine diesel engine: UMT vessel experimentation experience. *Glob. J. Inf. Technol. Comput. Sci.* **2012**, *1*, 1–7.
15. Lee, K.-J.; Shin, D.-S.; Lee, J.-P.; Yoo, D.-W.; Choi, H.-K.; Kim, H.-J. Hybrid photovoltaic/diesel green ship operating in standalone and grid-connected mode in South Korea-Experimental investigation. In Proceedings of the 2012 IEEE Vehicle Power and Propulsion Conference, Seoul, Korea, 9–12 October 2012; pp. 580–583.
16. Babu, S.; Jain, J.V. On-board solar power for small-scale distant-water fishing vessels. In Proceedings of the 2013 IEEE Global Humanitarian Technology Conference (GHTC), San Jose, CA, USA, 20–23 October 2013.

17. Cristea, O. Testing of PV module efficiency in naval conditions. In Proceedings of the 2013 8th International Symposium on Advanced Topics In Electrical Engineering (Atee), Bucharest, Romania, 23–25 May 2013.
18. Kirkpatrick, J.P. An Investigation of the Effectiveness of Solar Power on Navy Surface Combatants. Naval Post-Graduate School Monterey Ca. 2013. Available online: http://hdl.handle.net/10945/37652 (accessed on 1 November 2021).
19. Kobougias, I.C.; Tatakis, E.C.; Prousalidis, J. PV Systems Installed in Marine Vessels: Technologies and Specifications. *Adv. Power Electron.* **2013**, *2013*, 831560. [CrossRef]
20. Utama, I.K.A.P.; Santosa, P.I.; Chao, R.M.; Nasiruddin, A. New concept of solar-powered catamaran fishing vessel. In Proceeding of the 7th International Conference on Asian and Pasific Coasts, Hong Kong, 14–16 December 2011.
21. Yufang, Z.; Peng, Q.; Hong, Y. Fuel free ship, design for next generation. In Proceedings of the 2013 Eighth International Conference and Exhibition on Ecological Vehicles and Renewable Energies (EVER), Manhattan, NY, USA, 27–30 March 2013; pp. 1–5.
22. Alfonsín, V.; Suarez, A.; Cancela, A.; Sanchez, A.; Maceiras, R. Modelization of hybrid systems with hydrogen and renewable energy oriented to electric propulsion in sailboats. *Int. J. Hydrogen Energy* **2014**, *39*, 11763–11773. [CrossRef]
23. Cristea, O.; Popescu, M.-O.; Calinciuc, A.S. A correlation between simulated and real PV system in naval conditions. In Proceedings of the 2014 International Symposium on Fundamentals of Electrical Engineering (ISFEE), Manhattan, NY, USA, 28–29 November 2014; pp. 1–6.
24. Hussein, A.W.; Ahmed, M.W. Solar Energy: Solution to fuel dilemma. *Int. J. Res. Eng. Technol.* **2014**, *2*, 99–108.
25. Peng, C.; Shounan, S.; Hai, L.; Qiang, Z. Modeling and simulation of ship power system integration of solar energy. In Proceedings of the 2014 IEEE Conference and Expo Transportation Electrification Asia-Pacific (ITEC Asia-Pacific), Beijing, China, 31 August–3 September 2014; pp. 1–5.
26. Lan, H.; Wen, S.; Hong, Y.-Y.; Yu, D.C.; Zhang, L. Optimal sizing of hybrid PV/diesel/battery in ship power system. *Appl. Energy* **2015**, *158*, 26–34. [CrossRef]
27. Lan, H.; Dai, J.; Wen, S.; Hong, Y.Y.; Yu, D.C.; Bai, Y. Optimal tilt angle of photovoltaic arrays and economic alloca-tion of energy storage system on large oil tanker ship. *Energies* **2015**, *8*, 11515–11530. [CrossRef]
28. Tang, X.-J.; Wang, T.; Zhi, C.; Huang, Y.-M.; Xu-Jing, T. The design of power management system for solar ship. In Proceedings of the 2015 International Conference on Transportation Information and Safety (ICTIS), Wuhan, China, 25–28 June 2015; pp. 548–553.
29. Zhang, Y.; Sun, Y.; Luo, H.; Wang, Y. Study on effect of ship low frequency vibration on the output characteristics of PV cells under different solar irradiation. In Proceedings of the 2015 International Conference on Renewable Energy Research and Applications (ICRERA), Palermo, Italy, 22–25 November 2015; pp. 388–392.
30. Wen, S.; Lan, H.; Hong, Y.-Y.; Yu, D.C.; Zhang, L.; Cheng, P. Allocation of ESS by interval optimization method considering impact of ship swinging on hybrid PV/diesel ship power system. *Appl. Energy* **2016**, *175*, 158–167. [CrossRef]
31. Salleh, N.A.S.; Muda, W.M.W.; Abdullah, S.S. Feasibility study of optimization and economic analysis for grid-connected renewable energy electric boat charging station in Kuala Terengganu. In Proceedings of the 2015 IEEE Conference on Energy Conversion (CENCON), Johor Bahru, Malaysia, 19–20 October 2015; pp. 510–515.
32. Jia, J.; Dong, H. Research on ship power plant simulation system based on LabVIEW and MATLAB mixed program-ming. In Proceedings of the 2017 IEEE 2nd Information Technology, Networking, Electronic and Automation Control Conference (ITNEC), Chengdu, China, 15–17 December 2017.
33. Tang, R.L.; Wu, Z.; Fang, Y.J. Withdrawn: Design of Green Ships with Large-Scale Photovoltaic Arrays and Intelli-Gent MPPT Control. *Appl. Energy* **2017**. [CrossRef]
34. Yuan, Y.; Wang, J.; Yan, X.; Li, Q.; Long, T. A design and experimental investigation of a largescale solar ener-gy/diesel generator powered hybrid ship. *Energy* **2018**, *165*, 965–978. [CrossRef]
35. The Rise of Solar-Powered Yachts With Unlimited Range. Available online: https://citimarineyachts.com/technology/the-rise-of-solar-powered-yachts-with-unlimited-range/ (accessed on 30 September 2021).
36. Al-Rashed, A.A.; Oztop, H.F.; Kolsi, L.; Boudjemline, A.; Almeshaal, M.A.; Ali, M.E.; Chamkha, A. CFD study of heat and mass transfer and entropy generation in a 3D solar distiller heated by an internal column. *Int. J. Mech. Sci.* **2019**, *152*, 280–288. [CrossRef]
37. Sözen, A.; Şirin, C.; Khanlari, A.; Tuncer, A.D.; Gürbüz, E.Y. Thermal performance enhancement of tube-type alterna-tive indirect solar dryer with iron mesh modification. *Solar Energy* **2020**, *207*, 1269–1281. [CrossRef]
38. Selimefendigil, F.; Öztop, H.F. Performance assessment of a thermoelectric module by using rotating circular cylinders and nanofluids in the channel flow for renewable energy applications. *J. Clean. Prod.* **2021**, *279*, 123426. [CrossRef]
39. Ghasemi, S.E.; Ahangar, G.H.R.M. Numerical analysis of performance of solar parabolic trough collector with Cu-Water nanofluid. *Int. J. Nano Dimens.* **2014**, *5*, 233–240.
40. Subramani, J.; Sevvel, P.; Anbuselvam; Srinivasan, S. Influence of CNT coating on the efficiency of solar parabolic trough collector using AL_2O_3 nanofluids—A multiple regression approach. *Mater. Today Proc.* **2021**, *45*, 1857–1861. [CrossRef]
41. Hachicha, A.A.; Said, Z.; Rahman, S.; Al-Sarairah, E. On the thermal and thermodynamic analysis of parabolic trough collector technology using industrial-grade MWCNT based nanofluid. *Renew. Energy* **2020**, *161*, 1303–1317. [CrossRef]
42. Bellos, E.; Tzivanidis, C.; Said, Z. A systematic parametric thermal analysis of nanofluid-based parabolic trough solar collectors. *Sustain. Energy Technol. Assess.* **2020**, *39*, 100714. [CrossRef]
43. Abed, N.; Afgan, I.; Cioncolini, A.; Iacovides, H.; Nasser, A.; Mekhail, T. Thermal performance evaluation of various nanofluids with non-uniform heating for parabolic trough collectors. *Case Stud. Therm. Eng.* **2020**, *22*, 100769. [CrossRef]

44. Subhedar, D.G.; Chauhan, K.V.; Patel, K.; Ramani, B.M. Performance improvement of a conventional single slope single basin passive solar still by integrating with nanofluid-based parabolic trough collector: An experimental study. *Mater. Today Proc.* **2020**, *26*, 1478–1481. [CrossRef]
45. Bezaatpour, M.; Rostamzadeh, H.; Bezaatpour, J. Hybridization of rotary absorber tube and magnetic field inducer with nanofluid for performance enhancement of parabolic trough solar collector. *J. Clean. Prod.* **2021**, *283*, 124565. [CrossRef]
46. Rejeb, O.; Ghenai, C.; Bettayeb, M. Modeling and simulation analysis of solar absorption chiller driven by nanofluid-based parabolic trough collectors (PTC) under hot climatic conditions. *Case Stud. Therm. Eng.* **2020**, *19*, 100624. [CrossRef]
47. Peng, H.; Guo, W.; Li, M. Thermal-hydraulic and thermodynamic performances of liquid metal based nanofluid in parabolic trough solar receiver tube. *Energy* **2020**, *192*, 116564. [CrossRef]
48. Minea, A.A.; El-Maghlany, W.M. Influence of hybrid nanofluids on the performance of parabolic trough collectors in solar thermal systems: Recent findings and numerical comparison. *Renew. Energy* **2018**, *120*, 350–364. [CrossRef]
49. O'Keeffe, G.; Mitchell, S.; Myers, T.; Cregan, V. Time-dependent modelling of nanofluid-based direct absorption parabolic trough solar collectors. *Sol. Energy* **2018**, *174*, 73–82. [CrossRef]
50. Ellahi, R.; Alamri, S.Z.; Basit, A.; Majeed, A. Effects of MHD and slip on heat transfer boundary layer flow over a moving plate based on specific entropy generation. *J. Taibah Univ. Sci.* **2018**, *12*, 476–482. [CrossRef]
51. Alamri, S.Z.; Khan, A.A.; Azeez, M.; Ellahi, R. Effects of mass transfer on MHD second grade fluid towards stretching cylinder: A novel perspective of Cattaneo–Christov heat flux model. *Phys. Lett. A* **2019**, *383*, 276–281. [CrossRef]
52. Safaei, M.R.; Goshayeshi, H.R.; Chaer, I. Solar Still Efficiency Enhancement by Using Graphene Oxide/Paraffin Nano-PCM. *Energies* **2019**, *12*, 2002. [CrossRef]
53. Sarafraz, M.; Safaei, M.R. Diurnal thermal evaluation of an evacuated tube solar collector (ETSC) charged with graphene nanoplatelets-methanol nano-suspension. *Renew. Energy* **2019**, *142*, 364–372. [CrossRef]
54. Ellahi, R.; Zeeshan, A.; Abbas, T.; Hussain, F. Thermally Charged MHD Bi-Phase Flow Coatings with Non-Newtonian Nanofluid and Hafnium Particles along Slippery Walls. *Coatings* **2019**, *9*, 300. [CrossRef]
55. Sarafraz, M.M.; Tlili, I.; Tian, Z.; Bakouri, M.; Safaei, M.R. Smart optimization of a thermosyphon heat pipe for an evacuated tube solar collector using response surface methodology (RSM). *Phys. A* **2019**, *534*, 122146. [CrossRef]
56. Eid, M.R.; Mahny, K.; Al-Hossainy, A.F. Homogeneous-heterogeneous catalysis on electromagnetic radiative Prandtl fluid flow: Darcy-Forchheimer substance scheme. *Surf. Interfaces* **2021**, *24*, 101119. [CrossRef]
57. Maithani, R.; Kumar, A.; Zadeh, P.G.; Safaei, M.R.; Gholamalizadeh, E. Empirical correlations development for heat transfer and friction factor of a solar rectangular air passage with spherical-shaped turbulence promoters. *J. Therm. Anal. Calorim.* **2020**, *139*, 1195–1212. [CrossRef]
58. Elelamy, A.F.; Elgazery, N.S.; Ellahi, R. Blood flow of MHD non-Newtonian nanofluid with heat transfer and slip effects: Application of bacterial growth in heart valve. *Int. J. Numer. Meth.* **2020**, *30*, 4883–4908. [CrossRef]
59. Goshayeshi, H.R.; Safaei, M.R. Effect of absorber plate surface shape and glass cover inclination angle on the performance of a passive solar still. *Int. J. Numer. Meth.* **2020**, *30*, 3183–3198. [CrossRef]
60. Jathar, L.D.; Ganesan, S.; Shahapurkar, K.; Soudagar, M.E.M.; Mujtaba, M.A.; Anqi, A.E.; Farooq, M.; Khidmatgar, A.; Goodarzi, M.; Safaei, M.R. Effect of various factors and diverse approaches to enhance the performance of solar stills: A comprehensive review. *J. Therm. Anal. Calorim.* **2021**, 1–32. [CrossRef]
61. Khosravi, R.; Rabiei, S.; Khaki, M.; Safaei, M.R.; Goodarzi, M. Entropy generation of graphene–platinum hybrid nanofluid flow through a wavy cylindrical microchannel solar receiver by using neural networks. *J. Therm. Anal. Calorim.* **2021**, *145*, 1949–1967. [CrossRef]
62. Jamshed, W.; Devi, S.U.S.; Goodarzi, M.; Prakash, M.; Nisar, K.S.; Zakarya, M.; Abdel-Aty, A.H. Evaluating the unsteady Casson nanofluid over a stretching sheet with solar thermal radiation: An optimal case study. *Case Stud. Therm. Eng.* **2021**, *26*, 101148. [CrossRef]
63. Wang, Q.; Pei, G.; Yang, H. Techno-economic assessment of performance-enhanced parabolic trough receiver in concentrated solar power plants. *Renew. Energy* **2021**, *167*, 629–643. [CrossRef]
64. Wang, Q.; Shen, B.; Huang, J.; Yang, H.; Pei, G.; Yang, H. A spectral self-regulating parabolic trough solar receiver integrated with vanadium dioxide-based thermochromic coating. *Appl. Energy* **2021**, *285*, 116453. [CrossRef]
65. Tyagi, S.K.; Wang, S.W.; Singhal, M.K.; Kaushik, S.C.; Park, S.R. Exergy analysis and parametric study of concentrating type solar collectors. *Int. J. Therm. Sci.* **2007**, *46*, 1304–1310. [CrossRef]
66. Smit, S.; Kessels, W. Variational method for the minimization of entropy generation in solar cells. *J. Appl. Phys.* **2015**, *117*, 134504. [CrossRef]
67. Gupta, M.; Kaushik, S. Exergetic performance evaluation and parametric studies of solar air heater. *Energy* **2008**, *33*, 1691–1702. [CrossRef]
68. Ebrahimi-Moghadam, A.; Mohseni-Gharyehsafa, B.; Farzaneh-Gord, M. Using artificial neural network and quadratic algorithm for minimizing entropy generation of Al_2O_3-EG/W nanofluid flow inside parabolic trough solar collector. *Renew. Energy* **2018**, *129*, 473–485. [CrossRef]
69. Mwesigye, A.; Huan, Z.; Meyer, J.P. Thermal performance and entropy generation analysis of a high concentration ratio parabolic trough solar collector with Cu-Therminol®VP-1 nanofluid. *Energy Convers. Manag.* **2016**, *120*, 449–465. [CrossRef]

70. Akbarzadeh, S.; Valipour, M.S. Energy and exergy analysis of a parabolic trough collector using helically corrugated ab-sorber tube. *Renew. Energy* **2020**, *155*, 735–747. [CrossRef]
71. Jamshed, W.; Aziz, A. A comparative entropy based analysis of Cu and Fe_3O_4/methanol Powell-Eyring nanofluid in solar thermal collectors subjected to thermal radiation, variable thermal conductivity and impact of different nanoparticles shape. *Results Phys.* **2018**, *9*, 195–205. [CrossRef]
72. Aziz, A.; Jamshed, W.; Aziz, T. Mathematical model for thermal and entropy analysis of thermal solar collectors by using Maxwell nanofluids with slip conditions, thermal radiation and variable thermal conductivity. *Open Phys.* **2018**, *16*, 123–136. [CrossRef]
73. Mukhtar, T.; Jamshed, W.; Aziz, A.; Al-Kouz, W. Computational investigation of heat transfer in a flow subjected to magnetohydrodynamic of Maxwell nanofluid over a stretched flat sheet with thermal radiation. *Numer. Methods Partial. Differ. Equ.* **2020**, 1–21. [CrossRef]
74. Jamshed, W.; Shahzad, F.; Safdar, R.; Sajid, T.; Eid, M.R.; Nisar, K.S. Implementing renewable solar energy in presence of Maxwell nanofluid in parabolic trough solar collector: A computational study. *Waves Random Complex Media* **2021**, 1–32. [CrossRef]
75. Jamshed, W.; Devi, S.U.S.; Safdar, R.; Redouane, F.; Nisar, K.S.; Eid, M.R. Comprehensive analysis on copper-iron (II, III)/oxide-engine oil Casson nanofluid flowing and thermal features in parabolic trough solar collector. *J. Taibah Univer. Sci.* **2021**, *15*, 619–636. [CrossRef]
76. Jamshed, W. Thermal augmentation in solar aircraft using tangent hyperbolic hybrid nanofluid: A solar energy application. *Energy Environ.* **2021**, 1–44. [CrossRef]
77. Jamshed, W.; Nisar, K.S.; Ibrahim, R.W.; Shahzad, F.; Eid, M.R. Thermal expansion optimization in solar aircraft using tangent hyperbolic hybrid nanofluid: A solar thermal application. *J. Mater. Res. Technol.* **2021**, *14*, 985–1006. [CrossRef]
78. Jamshed, W.; Eid, M.R.; Mohd Nasir, N.A.A.; Nisar, K.S.; Aziz, A.; Shahzad, F.; Saleel, C.A.; Shukla, A. Thermal examination of renewable solar energy in parabolic trough solar collector utilizing Maxwell nanofluid: A noble case study. *Case Stud. Therm. Eng.* **2021**, *27*, 101258. [CrossRef]
79. Jamshed, W. Numerical investigation of MHD impact on Maxwell nanofluid. *Int. Commun. Heat Mass Transf.* **2021**, *120*, 104973. [CrossRef]
80. Brewster, M.Q. *Thermal Radiative Transfer and Properties*; John Wiley and Sons: Hoboken, NJ, USA, 1992.
81. Muhammad, K.; Hayat, T.; Alsaedi, A.; Ahmed, B. A comparative study for convective fow of basefuid (gasoline oil), nanomaterial (SWCNTs) and hybrid nanomaterial (SWCNTs + MWCNTs). *Appl. Nanosci.* **2020**, *11*, 9–20. [CrossRef]
82. Jamshed, W.; Nisar, K.S.; Ibrahim, R.W.; Mukhtar, T.; Vijayakumar, V.; Ahmed, F. Computational frame work of Cattaneo-Christov heat flux effects on Engine Oil based Williamson hybrid nanofluids: A thermal case study. *Case Stud. Therm. Eng.* **2021**, *26*, 101179. [CrossRef]
83. Aziz, A.; Jamshed, W.; Aziz, T.; Bahaidarah, H.M.S.; Rehman, K.U. Entropy analysis of Powell–Eyring hybrid nanofluid including effect of linear thermal radiation and viscous dissipation. *J. Therm. Anal. Calorim.* **2021**, *143*, 1331–1343. [CrossRef]
84. Das, S.; Chakraborty, S.; Jana, R.N. and Makinde, O.D. Entropy analysis of unsteady magnetonanofluid flow past accelerating stretching sheet with convective boundary condition. *Appl. Math. Mech.* **2015**, *36*, 1593–1610. [CrossRef]
85. Keller, H.B. *A New Difference Scheme for Parabolic Problems*; Hubbard, B., Ed.; Numerical Solutions of Partial Differential Equations; Academic Press: New York, NY, USA, 1971; pp. 327–350.
86. Wang, C.Y. Free convection on a vertical stretching surface. *Appl. Math. Mech.* **1989**, *69*, 418–420. [CrossRef]
87. Gorla, R.S.R.; Sidawi, I. Free convection on a vertical stretching surface with suction and blowing. *Flow Turbul. Combust.* **1994**, *52*, 247–257. [CrossRef]